Microstructural investigation into the damage mechanism of short pitch rail corrugation

Zhang, Pan; Li, Shaoguang; Ren, Fang; Hajizad, Omid; Dollevoet, Rolf; Li, Zili

DOI
10.1016/j.engfailanal.2025.109512

Publication date
2025

Document Version
Final published version

Published in
Engineering Failure Analysis

Engineering Failure Analysis 174 (2025) 109512

Contents lists available at ScienceDirect

Engineering Failure Analysis

journal homepage: www.elsevier.com/locate/engfailanal

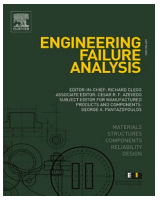

Microstructural investigation into the damage mechanism of short pitch rail corrugation

Pan Zhang, Shaoguang Li, Fang Ren, Omid Hajizad, Rolf Dollevoet, Zili Li *

Delft University of Technology, Section of Railway Engineering, Stevinweg 1, 2628 CN, Delft, the Netherlands

ARTICLE INFO

Keywords:
Rail corrugation
Microstructural analysis
Damage mechanism
Plastic deformation layer (PDL)
Differential wear
Rolling contact fatigue (RCF)

ABSTRACT

Short pitch corrugation is a typical rail defect that lacks a thorough understanding and adequate root-cause solutions. This paper aims to identify the damage mechanism of short pitch corrugation through a microstructural analysis of a field rail sample. This sample made of R260Mn pearlitic steel was taken from a straight section of the Dutch railway network, and its geometry and surface hardness variation along the corrugation were measured and analyzed. Eleven specimens, including both corrugated and non-corrugated zones, were sectioned from the rail sample and continuously examined using light optical microscopy, scanning electron microscopy and micro-hardness testing. The results indicate that the corrugation damage mechanism can be categorized into three stages: (1) pre-corrugation, characterized by uniform wear and plastic deformation; (2) corrugation initiation, dominated by differential wear; and (3) corrugation growth, involving both differential wear and plastic deformation accumulation. The initiation and growth of corrugation both contribute to an inhomogeneous distribution of plastic deformation layer (PDL) in the rail subsurface, which follows an approximately sinusoidal pattern, matching the corrugation geometry in both wavelength and phase. Consequently, the hardness also varies in phase with the corrugation geometry, with higher hardness values at corrugation peaks. In the non-corrugation zone, the PDL and hardness show relatively small and irregular fluctuations. This study also provides meaningful insights into rail grinding, suggesting that grinding should account for differential PDL thickness to prevent corrugation reoccurrence due to subsurface material inhomogeneity.

1. Introduction

Short pitch corrugation is a major type of rail defect in railway networks worldwide, which causes fierce vibration and noise, accelerates track deterioration, and considerably increases maintenance costs [1]. It appears as periodic undulations on the rail surface, with wavelengths falling in a short pitch range of 20–80 mm. Short pitch corrugation (hereafter, corrugation) primarily occurs on tangent tracks or in gentle curves [2], often recognised by shiny peaks and dark troughs. In practice, rail grinding has been widely used to treat corrugation, which, however, is costly, disrupts daily train operation, and cannot prevent corrugation reoccurrence [3]. Therefore, it is necessary to develop root-cause solutions to corrugation based on a thorough understanding of its formation mechanisms.

The corrugation formation process is generally understood as a feedback loop that consists of two primary features: the

* Corresponding author.
E-mail address: z.li@tudelft.nl (Z. Li).

https://doi.org/10.1016/j.engfailanal.2025.109512
Received 7 January 2025; Received in revised form 23 February 2025; Accepted 7 March 2025
Available online 8 March 2025

'wavelength-fixing' mechanism and the damage mechanism [2]. The 'wavelength-fixing' mechanism attempts to explain the origin of dynamic loads of vehicle-track systems that determine the corrugation wavelengths on the rail surface. Many hypotheses have been proposed in the literature, including pinned–pinned resonance [4], stick–slip [5,6], rail bending modes within the bogie distance [7–9], rail longitudinal vibration modes [10–12]and contact filter [13].

The corrugation damage mechanism, referring to the degradation of rail materials caused by dynamic loads, has received less attention in comparison to the 'wavelength-fixing' mechanism [14,15]. One possible reason is that the damage mechanism has been commonly assumed as differential wear. This assumption was mainly based on field observations that apparent wear marks occur on the corrugation troughs but not at peaks [2]. However, the microstructural analysis of corrugated rail material shows significantly differential plastic deformation at corrugation peaks and troughs [16,17], indicating that wear alone may not fully explain the corrugation development process. Numerical simulations in [18,19] also proposed that rail plastic deformation may play a critical role during corrugation growth. In addition, contradictory results from microstructural observations have been reported in [16,20,21] and [17,22] about whether corrugation peaks or troughs have thicker plastic deformation layers and higher hardness. Overall, the corrugation damage mechanism is complex and needs to be further investigated.

This paper aims to provide a better understanding of the corrugation damage mechanism through a comprehensive microstructural analysis of a field rail sample. Unlike previous studies that focus on some isolated locations (i.e., corrugation peaks or troughs), this work examines the continuous microstructural alterations along complete corrugation wave patterns. This approach allows us to correlate the microstructural variation in, e.g., μm, along corrugation with the spatial geometry in e.g., cm, offering a more thorough understanding of the microscopic damage mechanism in relation to the macroscopic wavelength. Moreover, this study compares the microstructural characteristics of both corrugated and non-corrugated zones to further clarify the damage mechanism.

The structure of this paper is organised as follows. Section 2 describes the field conditions and testing methods of a corrugated rail sample. Section 3 presents the experimental results of this sample, including corrugation geometry, microstructural features, and hardness distributions. Section 4 discusses the corrugation damage mechanism together with some numerical simulations. The main conclusions are summarised in Section 5.

2. Experimental details

This section introduces the field conditions of the rail corrugation sample, as well as the specimen preparation and testing methods for microscopic analysis.

2.1. Rail corrugation sample

The target corrugation sample was taken from the Dutch railway network between Mepple and Leeuwarden, as shown in Fig. 1. This sample was on a section of straight track and far away from the stations and curves. The characteristics of the track and the vehicle are summarised in Table 1. The ballasted track used standard UIC 54 rails, which were fixed on duo-block concrete sleepers by Deenik fastenings at every 0.6 m. The rails were made of R260Mn pearlitic steel, and its nominal chemical compositions and hardness are listed in Table 2. The annual traffic load was about 3.65 million gross tonnages (MGT), with the majority being passenger trains. The maximum operation speed was 140 km/h.

The rail corrugation was visually identified with shiny crests and dark valleys, as shown in Fig. 1. It followed a mature squat and disappeared after five distinguishable wave patterns in the traffic direction, suggesting that the corrugation was likely induced by large wheel-rail dynamic loads excited by the squat. This phenomenon was commonly observed in the Dutch railway network, and statistical data indicated that 41 % of rail squats induced corrugation wave patterns after them [23]. The corrugation wavelength was about 36 mm, falling in the typical short pitch range of 20–80 mm. RailProf was used to measure the vertical-longitudinal corrugation geometry

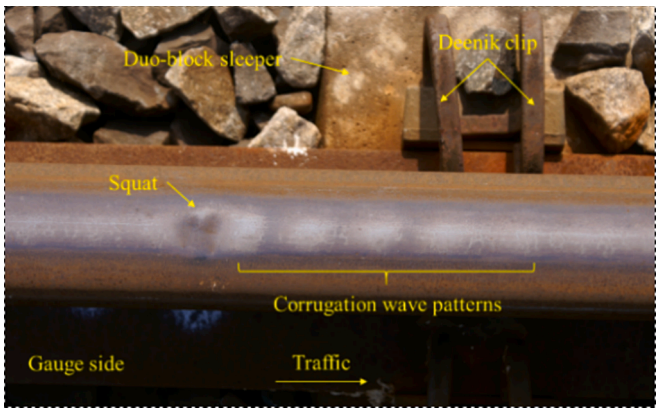

Fig. 1. Rail corrugation investigated in this study from the Dutch railway network. The corrugation was induced by a rail squat on a straight track with duo-block sleepers and Deenik fastening clips.

Table 1
The characteristics of the track and the vehicle.

Track	Rail	UIC 54, R260Mn
	Sleeper type	Duo-block concrete
	Sleeper spacing	0.6 *m*
	Fastening system	Deenik clip
	Railpad vertical stiffness	1300 MN/m
	Track layer	Ballast
	Curvature	Straight
Vehicle	Type	Mainly Passenger Train
	Speed	<=140 km/h
	Axel load	10 t
	Annual loads	3.65 MGT

Table 2
Nominal chemical composition (wt.%) and hardness of the rail steel [24].

Grade	C	Si	Mn	P	S	Hardness
R260Mn	0.55–0.75	0.15–0.60	1.30–1.70	<=0.025	<=0.025	~260 HB

along the railhead centre line at 5 mm intervals. The corrugation surface hardness was also tested along the traffic direction at 3 mm intervals using a hand-held DynMIC34247 hardness device (HB). Five parallel lines with a distance of 5 mm were measured in the running band, to ensure clear identification of the corrugation patterns, and it was found that the middle (third) line provided the best correlation with the corrugation geometry, as detailed in Section 3.1.

2.2. Rail specimens and test methods

To investigate the microstructural alterations and damage mechanisms of rail corrugation, eleven longitudinal-vertical specimens (S1, S2, …, S11) were prepared by cutting the rail sample along the center of the running band, as shown in Fig. 2. The dimensions of each specimen are 20 mm × 10 mm × 2 mm in the longitudinal (rolling), vertical and lateral directions, respectively. Based on their loading conditions, these specimens are categorized into three groups: the first group is located within the corrugation zone and is significantly influenced by impact loads from squats (e.g., S1 and S2); the second group is within the corrugation zone but is only slightly affected by squats (e.g., S5 and S6); and the third group is in the non-corrugation zone (e.g., S10 and S11). Specimen preparation followed standard metallographic procedures, including sectioning, embedding, polishing, and etching with a 3 % Nital solution.

The microstructures of each specimen were examined and recorded along the longitudinal direction at intervals of about 0.66 mm (corresponding to one image size) using an Olympus BH-2 light optical microscope (LOM), as shown in Fig. 3b. To investigate the mechanical properties of corrugated rail materials, micro-hardness tests were performed on each specimen at intervals of approximately 4 mm, at different depths: 0.1 mm, 0.25 mm, 0.5 mm, 1.0 mm, 2.0 mm, 3.0 mm, 7.0 mm, as shown in Fig. 3c. The testing device

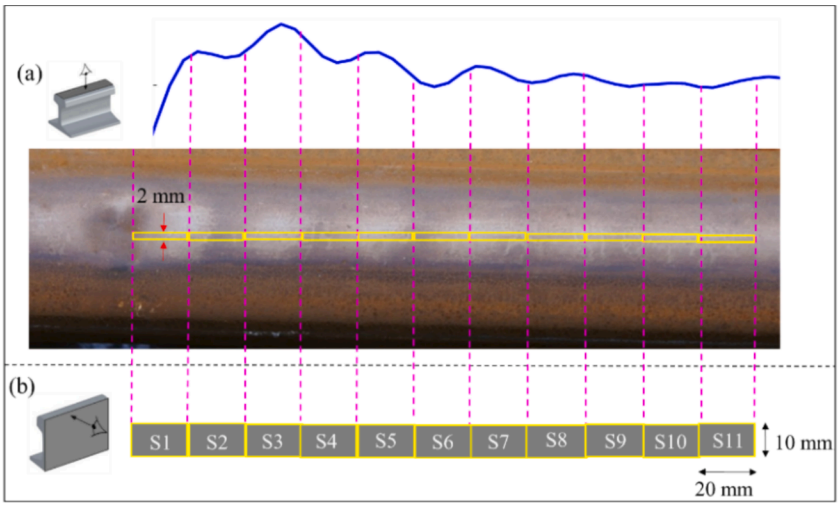

Fig. 2. The cutting scheme of eleven longitudinal-vertical specimens from the corrugated rail sample.

Fig. 3. Rail specimens and test methods. (a) rail specimens; (b) LOM; (c) micro-hardness test with remaining indentation marks in the specimen.

was Additionally, a JSM 6500F scanning electron microscope (SEM) was employed for higher-resolution imaging and more detailed microstructural analysis at selected regions of the specimens.

3. Results

This section presents experimental results, including the corrugation geometry and surface hardness, microstructural features of the corrugation specimens observed in LOM and SEM, and micro-hardness distribution at different locations and depths. The white etching layer (WEL) and brown etching layer (BEL) associated with the corrugated rail sample are also analyzed.

3.1. Corrugation geometry and surface hardness

Fig. 4 shows the measured corrugation geometry and surface hardness variation in the centre of the running band along the traffic direction. The corrugation peaks correspond to the shiny areas of the rail surface, while the troughs align with the darker regions. The corrugation has a wavelength of about 36 mm, corresponding to a corrugation frequency of about 1080 Hz with a train speed of 140 km/h. This wavelength falls within the range of 20–40 mm, a typical wavelength range of dynamic contact forces in the Dutch railway system [23]. The maximum peak-trough amplitude is about 18 μm at the first wave, which decreases rapidly in the traffic direction. After about 180 mm away from the squat, corrugation wave patterns become almost invisible.

The rail surface hardness also shows periodic fluctuations and is in phase with the corrugation geometry, consistent with the findings reported in [11,16,19]. The corrugation peaks generally correspond to prominent hardness peaks, reaching up to 382 HB, as indicated by the dashed lines in Fig. 4. The hardness difference between corrugation peaks and troughs suggests varying mechanical properties of rail materials along the corrugation, which resulted from different contact stress and work hardening at these locations induced by dynamic loads. Furthermore, the average surface hardness is around 320 HB, which is 1.23 times the nominal value of 260 HB for R260Mn grade steel. This increase in hardness indicates significant work hardening caused by plastic deformation in rail surface materials due to cyclic wheel-rail contacts. Similar to the corrugation geometry, after about 180 mm, the fluctuation of the surface hardness becomes less pronounced and more irregular, indicating a transition to a non-corrugated zone.

3.2. Microstructural features in OM and SEM

This subsection presents the microstructural characteristics of rail specimens in both corrugation and non-corrugation zones.

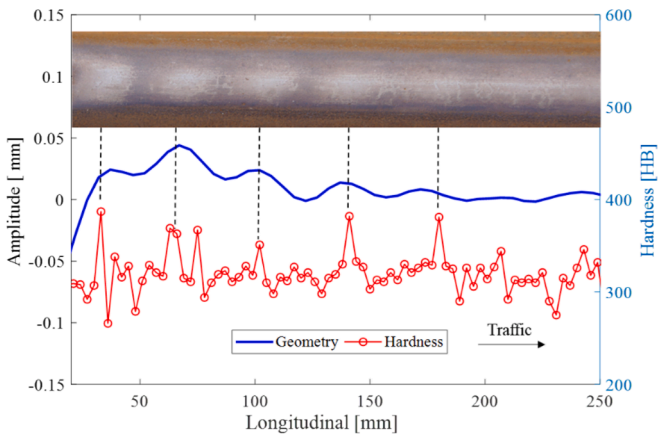

Fig. 4. The corrugation geometry and surface hardness in the centre of the running band.

Specimens S5 and S6 were selected for analysis of the corrugation zone because of their relatively large corrugation amplitudes with reduced influence from the squat impact loads suitable for a clearer assessment of corrugation-related microstructural changes. Meanwhile, specimens S10 and S11, located in the non-corrugated zone, are chosen as references to provide a baseline for the investigation of the microstructural changes and the associated damage mechanisms of corrugation.

3.2.1. Corrugation zone

Fig. 5 shows the LOM images of the rail microstructure at two locations: one at the corrugation peak of specimen S5 (Location A, Fig. 5a) and the other at the corrugation trough of specimen S6 (Location B, Fig. 5b). In Fig. 5a, a clear material plastic flow toward the traffic direction is observed from the running surface to a depth up to approximately 144.5 μm, indicating severe plastic deformation at the corrugation peak. Within this severe plastic deformation layer (PDL), the pearlite lamellae were realigned following the predominating shear stress directions during train passages [25,26]. The orientation of these deformed pearlites relative to the traffic direction gradually increases from about 10° near the surface to about 35° at a depth of 144.5 μm. Beneath this PDL, the microstructure of the bulk materials is less influenced by the dynamic loads. Fig. 5b shows that the PDL at the corrugation trough is much thinner than the peak, which is only about 37.0 μm. This result agrees with the microstructural observations of corrugated rail samples in [16,21].

Microstructural differences between the PDL and the original pearlite matrix are further examined using SEM at higher magnification, as shown in Fig. 6. Both regions show a typical lamellar structure composed of dark ferrite and white cementite bands. In the PDL (Fig. 6a), the lamellae are oriented at approximately 20° due to contact stresses, as indicated by the red arrows. In contrast, the lamellae within the pearlitic matrix are randomly oriented, highlighted by red dashed ovals in Fig. 6b. Additionally, the lamellar spacing in the PDL is observed to be smaller than that in the pearlite matrix. The spacing between cementite lamellae is a critical factor that influences the rail hardness and wear resistance. A smaller spacing, as observed in the PDL, suggests increased wear resistance compared to the original pearlitic structure of the rail material [27,28].

Fig. 7 shows the measurement of the PDL thickness in specimens S5 and S6 by OM, which covers a complete corrugation wave pattern. It can be seen that the PDL thickness fluctuates around 96 μm in the traffic direction, and gradually decreases from about 150 μm at the peak to 40 μm at the trough. The fitting curve reveals that this fluctuation follows an approximately sinusoidal pattern, aligning with the corrugation geometry in both wavelength and phase. However, it is noted that the peak-to-trough variation in PDL thickness is about 100 μm, significantly larger than the peak-to-trough amplitude (i.e., 14 μm shown in Fig. 4) of the corrugation geometry. The reason will be discussed in Section 4.

3.2.2. Non-corrugation zone

Fig. 8 presents LOM images of the rail microstructure at two locations in the non-corrugation zone: Location C in specimen S10 at 202 mm and Location D in specimen S11 at 233 mm. Similar to the observations in Fig. 5, both locations show two distinct layers: a PDL and an underlying pearlite matrix. However, unlike the significant PDL thickness differences in the corrugation zone, the PDL thickness at these two locations is relatively comparable, around 81.5 μm at Location C and 74.8 μm at Location D.

Fig. 9 further shows the PDL thickness in specimens S10 and S11 using OM along with the corresponding rail geometry. In this non-corrugation zone, the average PDL thickness is approximately 78 μm, which is thinner than that observed in the corrugation zone. Besides, the PDL thickness in this region shows only slight and random fluctuations, unlike the strong variation consistent with corrugation geometry in Fig. 7. The fitted trend line follows a nearly linear pattern, indicating uniform plastic deformation in the non-corrugation zone. Notably, a pronounced peak is observed at around 218 mm, corresponding to a thick mixed layer of WEL and BEL, which will be shown in Section 3.4.

3.3. Micro-hardness results

Fig. 10 shows the micro-hardness distribution at depths of 0.1 mm and 0.25 mm along the traffic direction, against the corresponding corrugation geometry. It can be seen that the hardness values at both depths fluctuate around 300 HV, but they follow

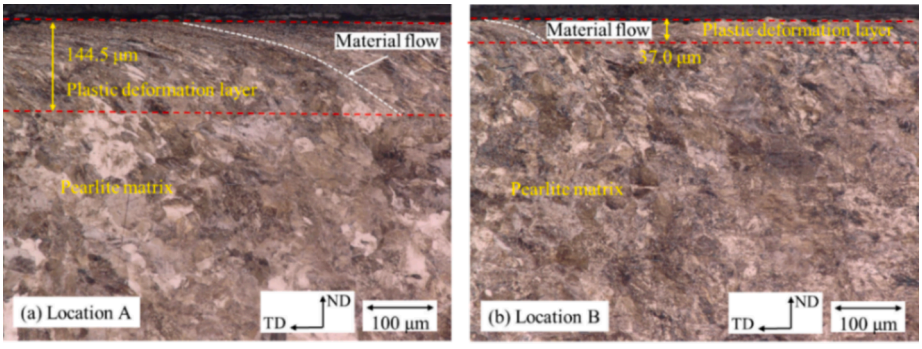

Fig. 5. OM images of the rail microstructure at (a) Location A, the corrugation peak of specimen S5; (b) Location B, the corrugation trough of specimen S6. ND indicates the normal direction and TD traffic direction.

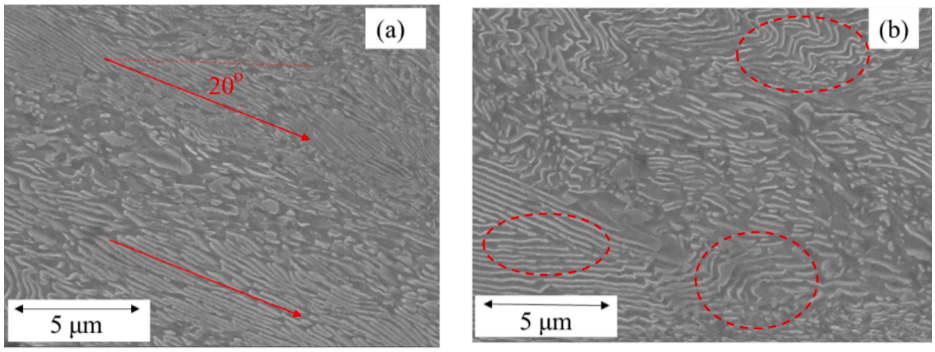

Fig. 6. SEM micrographs in (a) the severe plastic deformation layer; and (b) the original pearlite matrix.

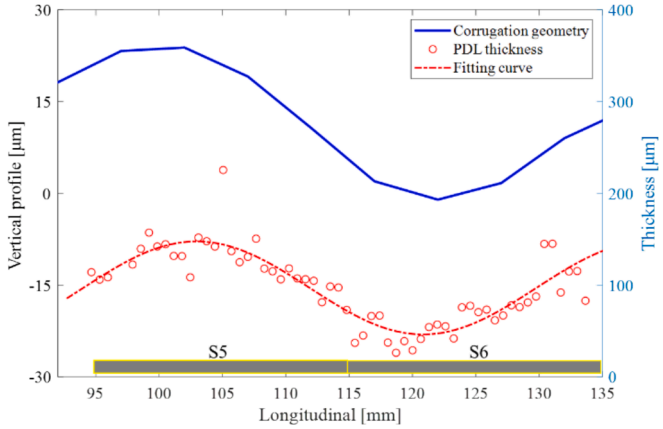

Fig. 7. The thickness of the plastic deformation layer at specimens S5 and S6 in the corrugation zone.

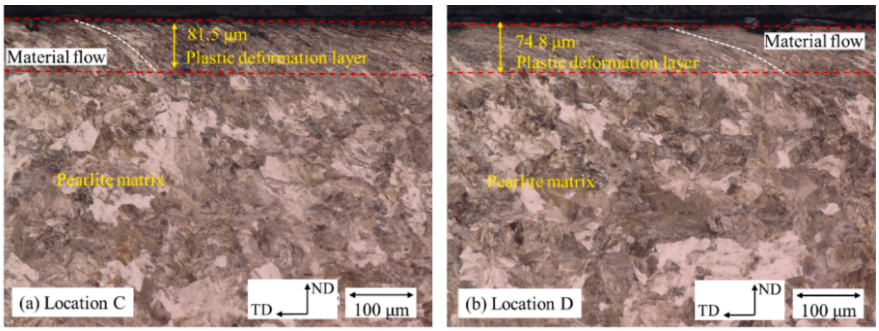

Fig. 8. OM images of the rail microstructure at (a) Location C in specimen S10 at 202 mm; and (b) Location D in specimen S11 at 233 mm. ND indicates the normal direction and TD traffic direction.

different patterns. At a depth of 0.1 mm, hardness peaks generally align with the corrugation peaks, as indicated by the vertical grey dashed lines. In contrast, the hardness at 0.25 mm depth shows relatively random variation without a clear correlation with the corrugation geometry. This suggests that the corrugation-affected zone, where differential plastic deformation and material hardening occur, reaches at least 0.1 mm deep but less than 0.25 mm. This finding aligns with the LOM observations in Fig. 7, where the PDL thickness at the corrugation peak is between 0.1 mm and 0.15 mm. Additionally, when compared to the variation trend of the surface hardness in Fig. 4, the subsurface hardness fluctuation at 0.1 mm depth is generally in phase but less pronounced, suggesting an attenuating influence of corrugation with increasing depth. Furthermore, a notable hardness peak is observed at around 39 mm, reaching up to 550 HV. This peak is caused by the presence of a thick mixture of WEL and BEL at this position, which will be presented in more detail in Section 3.4.

In practice, rail grinding has been commonly employed to treat corrugation by removing a layer of materials from the rail surface.

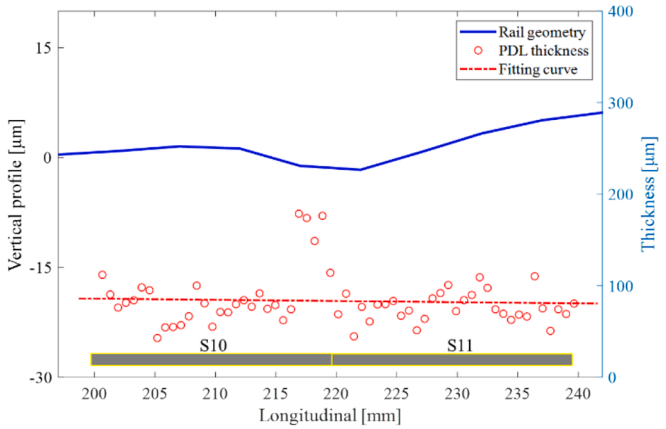

Fig. 9. The thickness of the plastic deformation layer at specimens S10 and S11 in the non-corrugation zone.

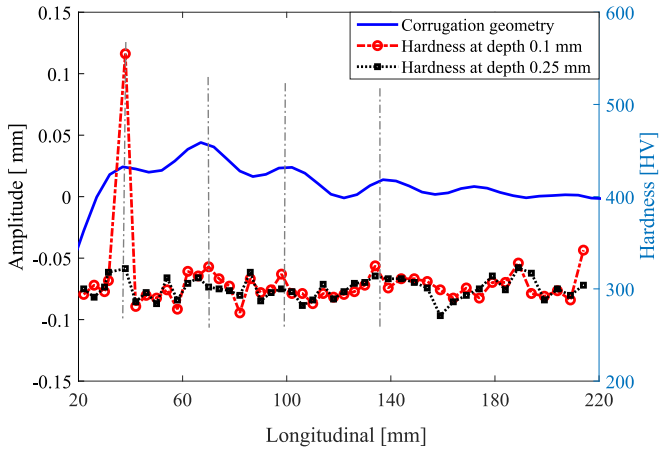

Fig. 10. Micro-hardness distribution in the traffic direction together with the corrugation geometry.

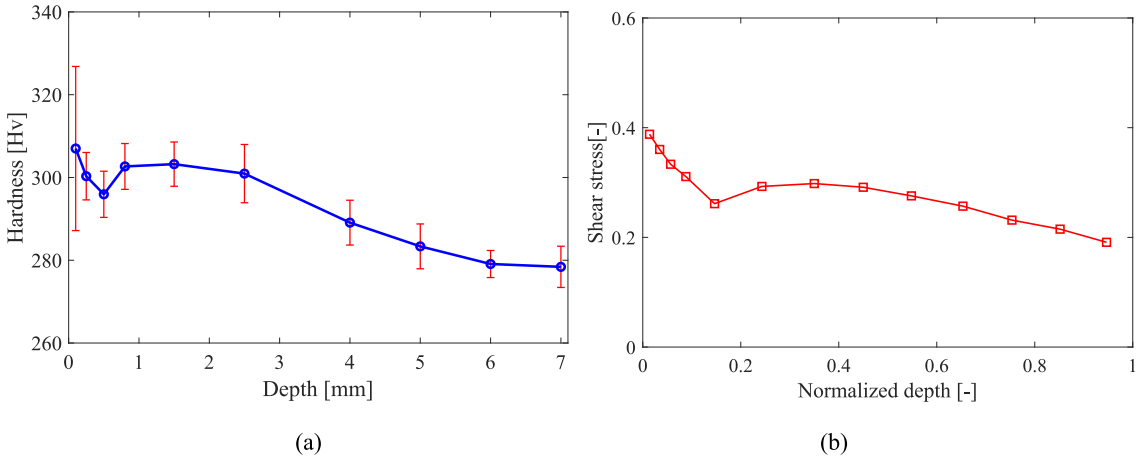

Fig. 11. Micro hardness distribution in comparison with shear stress distribution along the rail depth. (a) Micro hardness distribution from measurement; (b) simulated shear stress distribution from [29]. The shear stress is normalized by normal pressure, and the depth is normalized by the semi-axis of the wheel–rail contact area.

The findings in Fig. 7 and Fig. 10 provide insights into determining the appropriate grinding depth. It can be seen that the depth of the corrugation-affected zone is over 0.1 mm, considerably deeper than the measured corrugation amplitude. Therefore, the rail grinding depth is suggested to account for the differential PDL thickness (see Fig. 7) to prevent corrugation reoccurrence due to subsurface material inhomogeneity.

Fig. 11 shows the hardness distribution at different depths of the rail specimens: 0.1 mm, 0.25 mm, 0.5 mm, 1.0 mm, 2.0 mm, 3.0 mm, and 7.0 mm. Each data point and corresponding red bar represent the average hardness and standard deviation between 20 mm and 220 mm along the depth. At the depth of 0.1 mm, the hardness is approximately 307 HV. From 0.1 mm to 0.5 mm, the hardness drops to a local minimum of about 296 HV, then rises to 301–303 HV between 1.0 mm and 2.5 mm. Beyond 2.5 mm, the hardness gradually decreases, reaching about 279 HV at a depth of 6.0 mm. Below 6 mm, the hardness remains almost constant at 278 HV, close to the nominal hardness value of R260MN pearlitic steel.

These hardness variations with depth are caused by the wheel-rail contact and the resulting subsurface stress distribution. It is found that the hardness pattern shown in Fig. 11a closely aligns with the maximum shear stress distributions of the rail subsurface under the contact patch in Fig. 11b [25,29], confirming that shear stress plays a significant role in the work hardening and plastic deformation of rail materials. The highest hardness at 0.1 mm depth is due to the proximity to the wheel-rail interface, where it experiences the largest shear stress from traction forces. This surface layer also shows the largest deviation in hardness, likely due to dynamic loading from corrugation and the presence of BEL and WEL at certain locations. Deeper into the rail, a typical 'kink' is observed in the shear stress distribution [29], corresponding to a hardness trough at around 0.5 mm depth and a peak between 1 mm and 2.5 mm. Beyond 2.5 mm, as the shear stress decreases, the hardness gradually declines until it reaches the hardness of bulk materials. Similar results of pearlitic rails in UK railway lines have been reported in [30].

3.4. WEL and BEL

In Figs. 9 and 10, notable hardness peaks are observed around 218 mm and 39 mm, respectively. These anomalies are caused by the presence of a mixture of WEL and BEL, as depicted in Fig. 12. WEL and BEL, which appear white and brown under OM after etching, are significantly harder and more brittle than the bulk matrix [24,31]. The WEL in Fig. 12a has a thickness of approximately 32.4 μm, while the BEL is 69.1 μm thick. A 70 μm-long crack is present within both layers, with an orientation of about 80°, and it had not propagated into the underlying pearlite structure. Fig. 12b shows the WEL is thinner at 14.7 μm, with a thicker BEL of 117.5 μm, and no micro-cracks are observed.

WEL and BEL have been considered possible causes of crack initiation of rolling contact fatigue (RCF) [24,32]. The formation mechanism of WEL has been extensively studied, and it could be mechanically or thermomechanically induced [33–35]. With limited studies in the literature, BEL remains less understood. It is found in [24] that compared to WEL, the cracks formed in the BEL tend to propagate deeper into the materials without branching. While this work is not intended to identify the formation mechanism of WEL and BEL, some insights have been gained from observations of the rail specimens.

It is found that WEL and BEL can either coexist, as shown in Fig. 12, or occur independently. When they coexist, BEL typically forms between the upper WEL and lower pearlite matrix, suggesting that BEL may represent a transitional state from the pearlite structure to the WEL. Fig. 12 also shows that the boundaries between WEL and BEL are relatively smooth, while the boundaries between BEL and the pearlite matrix are more irregular. Similar phenomena are observed in Australian pearlitic rails [33]. The size of these irregularities is comparable to the pearlite grain or colony sizes, indicating that the formation of BEL may be related to the changes of these pearlitic structures due to mechanical or thermal–mechanical loading. Besides, previous studies have primarily reported the occurrence of WEL at corrugation peaks [16,21]. However, through continuous OM observations, we found that WEL and BEL can form not only at the peaks but also at troughs and along the slopes of corrugation. This phenomenon could be explored further in future studies.

4. Discussions

4.1. Corrugation damage mechanism

Based on the microstructural analysis in this work and the numerical simulations in [10,19], the corrugation damage mechanism is identified as four phases, as depicted by a schematic drawing in Fig. 13. At the beginning (Phase I), the rail is new without damage, as shown in Fig. 13a. After certain load cycles before corrugation initiates, the rail surface is worn uniformly and a homogeneous PDL forms, as shown in Fig. 13b. The formation of PDL could possibly be caused by the contact surface asperities that leads to local stress concentration and a much higher pressure than smooth-surface contact [36]. This phase (II) is referred to as 'pre-corrugation damage', supported by the microstructural observations of the non-corrugation zone in Figs. 8 and 9. Afterwards, an initial excitation starts to take notable effects in the vehicle-rack system, causing longitudinal dynamic force, visible accumulation of differential wear, and corrugation initiation [10], as shown in Fig. 13c. Differential wear means that rail wear is more at corrugation troughs than peaks, which results in a thinner PDL at the troughs. This is consistent with the observations in Fig. 7, where the PDL thickness follows an approximately sinusoidal pattern, in phrase with the corrugation geometry. This phase (III) is referred to as 'corrugation initiation damage', primarily driven by differential wear.

With increasing accumulation of differential wear, corrugation continuously grows with larger amplitude, as shown in Fig. 13d. During this phase (IV), corrugation itself becomes an increasingly significant excitation to the vehicle-track system that causes larger vertical dynamic force, additional to the initial excitation [10]. Based on the numerical simulations in [19] with severe corrugation, the corrugation peaks experience higher residual stress and plastic strains compared to troughs, causing greater plastic deformation at

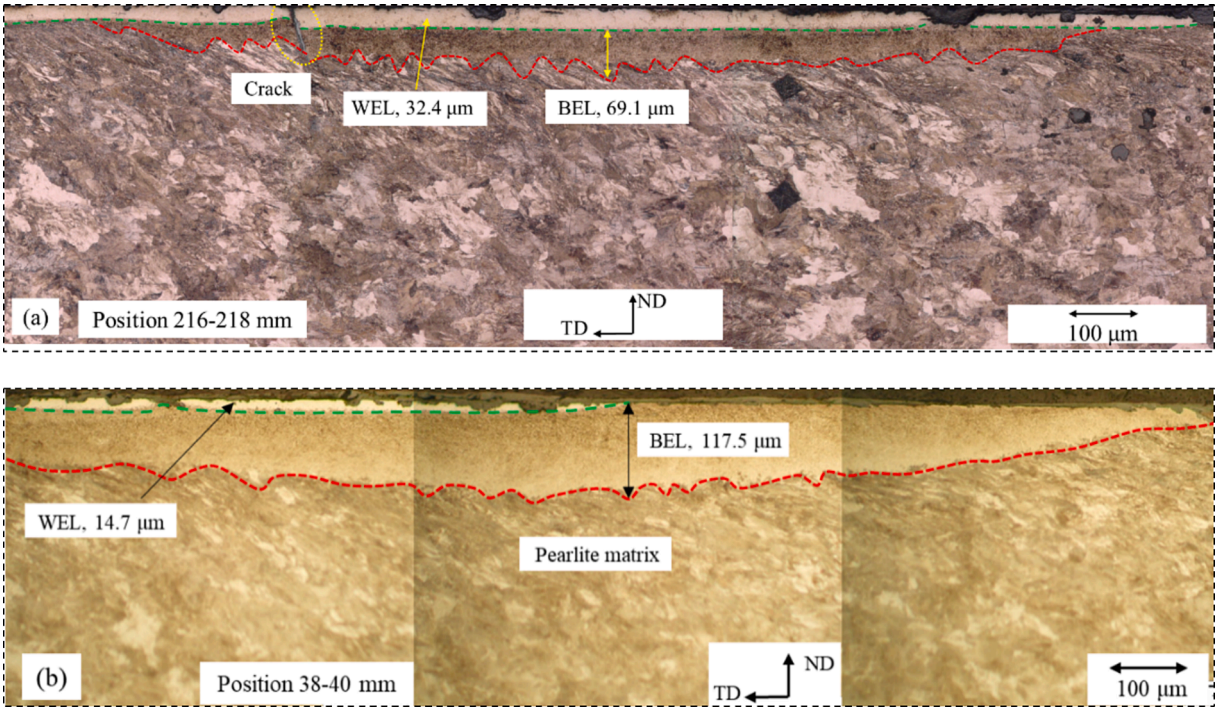

Fig. 12. A mixture of WEL and BEL at (a) 216–218 mm; (b) 38–40 mm. ND indicates the normal direction and TD traffic direction.

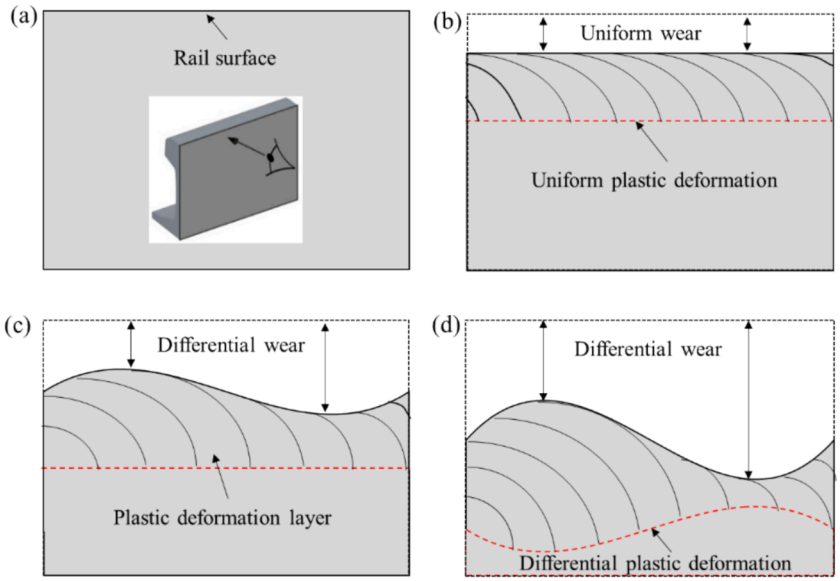

Fig. 13. The schematic drawing of the corrugation damage mechanism. (a) Phase I, new rail without damage; (b) Phase II, pre-corrugation damage with uniform wear and plastic deformation; (c) Phase III, corrugation initiation damage primarily driven by differential wear; (d) Phase IV, corrugation growth damage dominated by both differential wear and differential plastic deformation.

peaks. This explains the results in Fig. 7 why the peak-to-trough variation in PDL thickness (i.e., 100 μm) is significantly larger than the peak-to-trough amplitude of the corrugation geometry (i.e., 14 μm). This phase is called 'corrugation growth damage', dominated by both differential wear and differential plastic deformation accumulation.

4.2. The influence of loading conditions on corrugation damage mechanisms

In this study, it is observed that corrugation peaks correspond to thicker PDL and higher hardness, consistent with the findings in [11,21]. However, contradictory results are reported that corrugation troughs show greater plastic deformation thickness and hardness compared to the peaks [17,22]. A comparison of these results suggests that these discrepancies may arise from differing loading conditions. In this work, as well as in [11,21], corrugation develops on straight tracks with relatively low creep ratios and unsaturated traction forces. However, in [17,22], corrugation develops under saturated creep forces with high creep ratios of 7.5 % and 6 %, respectively, which typically occurs in curved tracks. The likely explanation is that under lower traction forces, differential wear is the dominant damage mechanism for corrugation initiation, as discussed in Section 4.1. In contrast, with larger creep forces, uneven plastic deformation becomes the primary mechanism [22]. Further investigation could be performed to better understand the influence of different loading conditions on the corrugation formation mechanisms.

5. Conclusions

This paper investigates the damage mechanism of short pitch corrugation through microstructural analysis of a field rail sample made of R260MN pearlite steel, taken from a straight track section on the Dutch railway network. Rail geometry and surface hardness were measured to evaluate their spatial variation along the corrugation profile. The rail was longitudinally sectioned along the traffic direction into eleven specimens, which were examined using LOM, SEM, and micro-hardness testing. The main findings are summarized as follows.

1. The damage mechanism of rail corrugation can be categorized into three stages: (1) pre-corrugation, characterized by uniform wear and plastic deformation; (2) corrugation initiation, dominated by differential wear; and (3) corrugation growth, involving both differential wear and plastic deformation.
2. The thickness of PDL in the corrugation zone follows an approximately sinusoidal pattern, matching the corrugation geometry in both wavelength and phase. In contrast, PDL thickness in the non-corrugation zone is nearly linear with limited fluctuation.
3. The pearlite lamellae within PDL were realigned due to the wheel-rail contact stress, with reduced lamellar spacing and increased hardness and wear resistance compared to the original pearlite structure.
4. The rail hardness varies in phase with the corrugation geometry, and corrugation peaks correspond to greater hardness values. This hardness fluctuation is the most pronounced at the surface and gradually decreases with depth.
5. Rail hardness distribution along the depth closely aligns with the maximum shear stress distributions in the rail subsurface, showing that shear stress plays a significant role in the work hardening of rail materials.
6. WEL and BEL can either coexist, or occur independently, and when they coexist, BEL typically forms between the upper WEL and lower pearlite matrix. The boundary between WEL and BEL is relatively smooth, whereas the boundary between BEL and the pearlite matrix is more irregular.

This study also provides practical guidance for rail grinding, suggesting that grinding depth should account for differential PDL thickness to prevent corrugation recurrence caused by subsurface material inhomogeneity. In future work, numerical simulation of the squat-induced corrugation in this work could be performed to better understand the development mechanism. In addition, the microstructural analysis of corrugation samples made of different rail materials could be conducted to examine the general applicability of the proposed damage mechanism.

CRediT authorship contribution statement

Pan Zhang: Writing – review & editing, Writing – original draft, Software, Methodology, Investigation, Formal analysis, Conceptualization. **Shaoguang Li:** Writing – review & editing, Formal analysis, Data curation, Conceptualization. **Fang Ren:** Writing – review & editing, Formal analysis, Data curation. **Omid Hajizad:** Writing – review & editing, Formal analysis, Data curation. **Rolf Dollevoet:** Resources, Project administration, Funding acquisition. **Zili Li:** Writing – review & editing, Supervision, Resources, Project administration, Investigation, Funding acquisition, Conceptualization.

Declaration of competing interest

The authors declare that they have no known competing financial interests or personal relationships that could have appeared to influence the work reported in this paper.

Data availability

Data will be made available on request.

References

[1] K. Oostermeijer, Review on short pitch rail corrugation studies, Wear 265 (2008) 1231–1237.

[2] S. Grassie, J. Kalousek, Rail corrugation: characteristics, causes and treatments, Proceedings of the Institution of Mechanical Engineers, Part f: Journal of Rail and Rapid Transit 207 (1993) 57–68.
[3] H. Tanaka, M. Miwa, Modeling the development of rail corrugation to schedule a more economical rail grinding, Proceedings of the Institution of Mechanical Engineers, Part f: Journal of Rail and Rapid Transit 234 (2020) 370–380.
[4] K. Hempelmann, K. Knothe, An extended linear model for the prediction of short pitch corrugation, Wear 191 (1996) 161–169.
[5] J. Kalousek, K. Johnson, An investigation of short pitch wheel and rail corrugations on the Vancouver mass transit system, Proceedings of the Institution of Mechanical Engineers, Part f: Journal of Rail and Rapid Transit 206 (1992) 127–135.
[6] P. Bao, X. Cui, H. Ding, Y. Yin, Z. Du, Z. Yang, Influences of friction self-excited vibration characteristics of various types of high-speed trains on rail corrugations in braking sections, Eng. Fail. Anal. 134 (2022) 106087.
[7] T. Wu, D. Thompson, An investigation into rail corrugation due to micro-slip under multiple wheel/rail interactions, Wear 258 (2005) 1115–1125.
[8] C. Ma, L. Gao, T. Xin, X. Cai, M.M. Nadakatti, P. Wang, The dynamic resonance under multiple flexible wheelset-rail interactions and its influence on rail corrugation for high-speed railway, J. Sound Vib. 498 (2021) 115968.
[9] G. Tao, Q. Yuan, X. Yang, X. Wu, Q. Xie, Q. Guan, W. Li, Z. Wen, On short-pitch rail corrugation of suburban express railway caused by localized rail-bending vibrations within the bogie wheelbase, International Journal of Rail Transportation (2025) 1–19.
[10] Z. Li, S. Li, P. Zhang, A. Núñez, R. Dollevoet, Mechanism of short pitch rail corrugation: initial excitation and frequency selection for consistent initiation and growth, International Journal of Rail Transportation (2022) 1–36.
[11] P. Zhang, Z. Li, Experimental study on the development mechanism of short pitch corrugation using a downscale V-Track test rig, Tribol. Int. 108293 (2023).
[12] P. Zhang, Z. Li, New experimental evidences of corrugation formation due to rail longitudinal vibration mode, International Journal of Rail Transportation (2024) 1–22.
[13] P. Bellette, P. Meehan, W. Daniel, Contact induced wear filtering and its influence on corrugation growth, Wear 268 (2010) 1320–1328.
[14] A. Saulot, S. Descartes, D. Desmyter, D. Levy, Y. Berthier, A tribological characterization of the “damage mechanism” of low rail corrugation on sharp curved track, Wear 260 (2006) 984–995.
[15] H. Zhang, S. Zhang, H. Zhong, W. Wang, E. Meli, X. Cui, H. Ding, Q. Liu, Damage mechanism of a long-wavelength corrugated rail associated with rolling contact fatigue, Eng. Fail. Anal. 136 (2022) 106173.
[16] E. Wild, L. Wang, B. Hasse, T. Wroblewski, G. Goerigk, A. Pyzalla, Microstructure alterations at the surface of a heavily corrugated rail with strong ripple formation, Wear 254 (2003) 876–883.
[17] S. Chen, G. Zhao, S. Liu, P. Wang, H. Wang, Study on the evolution of material microstructure and constitutive relation during rail corrugation development, Wear 532 (2023) 205123.
[18] Z. Wen, X. Jin, X. Xiao, Z. Zhou, Effect of a scratch on curved rail on initiation and evolution of plastic deformation induced rail corrugation, Int. J. Solids Struct. 45 (2008) 2077–2096.
[19] S. Li, M. Naeimi, C. He, R. Dollevoet, Z. Li, An integrated 3D dynamic FE vehicle-track model in elasto-plasticity to investigate short pitch corrugation under cyclic wheel loads, in: Structures, Elsevier, 2023, pp. 1000-1011.
[20] H. Feller, K. Walf, Surface analysis of corrugated rail treads, Wear 144 (1991) 153–161.
[21] M. Hiensch, J.C. Nielsen, E. Verheijen, Rail corrugation in The Netherlands—measurements and simulations, Wear 253 (2002) 140–149.
[22] Q. Liu, B. Zhang, Z. Zhou, An experimental study of rail corrugation, Wear 255 (2003) 1121–1126.
[23] Z. Li, R. Dollevoet, M. Molodova, X. Zhao, Squat growth—Some observations and the validation of numerical predictions, Wear 271 (2011) 148–157.
[24] S. Li, J. Wu, R.H. Petrov, Z. Li, R. Dollevoet, J. Sietsma, “Brown etching layer”: A possible new insight into the crack initiation of rolling contact fatigue in rail steels? Eng. Fail. Anal. 66 (2016) 8–18.
[25] A. Kapoor, J.H. Beynon, D. Fletcher, M. Loo-Morrey, Computer simulation of strain accumulation and hardening for pearlitic rail steel undergoing repeated contact, The, J. Strain Anal. Eng. Des. 39 (2004) 383–396.
[26] J.-P. Li, Y. Zhou, Z.-N. Cheng, C. Wang, Z.-Y. Weng, Evolution of microscopic characteristics of rolling contact fatigue coexisting with wear of U75V rail, Tribol. Int. 190 (2023) 109041.
[27] A.J. Perez-Unzueta, J.H. Beynon, Microstructure and wear resistance of pearlitic rail steels, Wear 162 (1993) 173–182.
[28] J. Wen, J. Marteau, S. Bouvier, M. Risbet, F. Cristofari, P. Secordel, Comparison of microstructure changes induced in two pearlitic rail steels subjected to a full-scale wheel/rail contact rig test, Wear 456 (2020) 203354.
[29] F. Ren, Z. Yang, Z. Li, An efficient 3D finite element procedure for simulating wheel–rail cyclic contact and ratcheting, Tribol. Int. 109878 (2024).
[30] F. Alwahdi, A. Kapoor, F. Franklin, Subsurface microstructural analysis and mechanical properties of pearlitic rail steels in service, Wear 302 (2013) 1453–1460.
[31] H.W. Zhang, S. Ohsaki, S. Mitao, M. Ohnuma, K. Hono, Microstructural investigation of white etching layer on pearlite steel rail, Mater. Sci. Eng. A 421 (2006) 191–199.
[32] J. Seo, S. Kwon, H. Jun, D. Lee, Numerical stress analysis and rolling contact fatigue of White Etching Layer on rail steel, Int. J. Fatigue 33 (2011) 203–211.
[33] B.H. Nguyen, E.T. Camacho, A. Al-Juboori, Y. Ma, H. Li, H. Zhu, Tribological behaviors of two distinct classes of white etching layers on rail surface, Wear 532 (2023) 205097.
[34] J. Wu, R.H. Petrov, M. Naeimi, Z. Li, R. Dollevoet, J. Sietsma, Laboratory simulation of martensite formation of white etching layer in rail steel, Int. J. Fatigue 91 (2016) 11–20.
[35] B.H. Nguyen, A. Al-Juboori, H. Zhu, A.A. Gazder, H. Li, K. Tieu, Fracture mechanisms in rails with mechanically and thermomechanically-induced white etching layers under three-point bending, Eng. Fail. Anal. 131 (2022) 105813.
[36] A. Kapoor, F. Franklin, S. Wong, M. Ishida, Surface roughness and plastic flow in rail wheel contact, Wear 253 (2002) 257–264.